Supplementary material: Spectroscopic signature of sublattice polarization in the lattice dynamics of an antiferroelectric crystal

E. Constable,[1,*] L. Bergen,[1] A. Shuvaev,[1] J. Wettstein,[1] L. Weymann,[1] E. Malysheva,[1] A. Pimenov,[1] and M. Guennou[2,†]

[1] *Institute of Solid State Physics, TU Wien, 1040 Vienna, Austria*

[2] *Department of Physics and Materials Science, University of Luxembourg, 41 rue du Brill, L-4422 Belvaux, Luxembourg*

SIMPLE DISPLACIVE ANTIFERROELECTRIC MODEL

To model the dynamics of a simplified displacive antiferroelectric, we consider the toy model system depicted in Fig. 1. Here, two equivalent masses ($m_a = m_b = m$) are constrained along two independent parallel axes x_a and x_b, each within a local Landau potential of the form,

$$U(x) = ax^2 + bx^4. \tag{1}$$

Temperature evolution of the potential is achieved by setting $a = a(T) = \alpha\,(T - T_\mathrm{c})$, accommodating the conventional second-order displacive transition at a critical temperature T_c.

The two masses are then allowed to interact in the simplest manner through the following model (or "interaction") potential,

$$U_\mathrm{F} = c(x_a - x_b)^2, \tag{2}$$

$$U_\mathrm{AF} = c(x_a + x_b)^2. \tag{3}$$

In this way, the model supports both a ferroelectric (U_F) and antiferroelectric (U_AF) ordering depending on the choice of interaction potential and by fixing $x_a = x_b$ in the case of a ferroelectric interaction and $x_a = -x_b$ for an antiferroelectric interaction. The total potential experienced by each mass is then defined as $U_\mathrm{tot} = U(x) + U_\mathrm{F,AF}$. It is depicted in Fig. 1(b) for the antiferroelectric case.

The equations of motion for each mass, including some linear damping, are then,

$$m\ddot{x}_a = -\gamma_a\dot{x}_a - \frac{\partial U_\mathrm{tot}}{\partial x_a}, \tag{4}$$

$$m\ddot{x}_b = -\gamma_b\dot{x}_b - \frac{\partial U_\mathrm{tot}}{\partial x_b}, \tag{5}$$

with

$$\frac{\partial U_\mathrm{tot}}{\partial x_a} = 2ax_a + 4bx_a^3 + 2c(x_a \mp x_b), \tag{6}$$

$$\frac{\partial U_\mathrm{tot}}{\partial x_b} = 2ax_b + 4bx_b^3 \mp 2c(x_a \mp x_b). \tag{7}$$

Here, the order of the signs refers to the case for ferroelectric and antiferroelectric interactions respectively. As we define the *"ordered"* phases by $x_a = x_b$ for the ferroelectric case and $x_a = -x_b$ for the antiferroelectric case, at static equilibrium the effects of the interaction potential cancel out. Neglecting damping, we find,

$$m\ddot{x}_a = -\frac{\partial U_\mathrm{tot}}{\partial x_a} = -x_a(2a + 4bx_a^2) = 0, \tag{8}$$

which has the trivial solution $x_a = 0$ and the non-trivial solution $2a + 4bx_a^2 = 0$ or,

$$x_a = \pm\sqrt{\frac{-a}{2b}}. \tag{9}$$

Solutions for the second mass can be obtained similarly with the substitution $x_b = \pm x_a$ depending on the interaction. This is the standard result for a second-order phase transition with real solutions for $a < 0$. It has been well

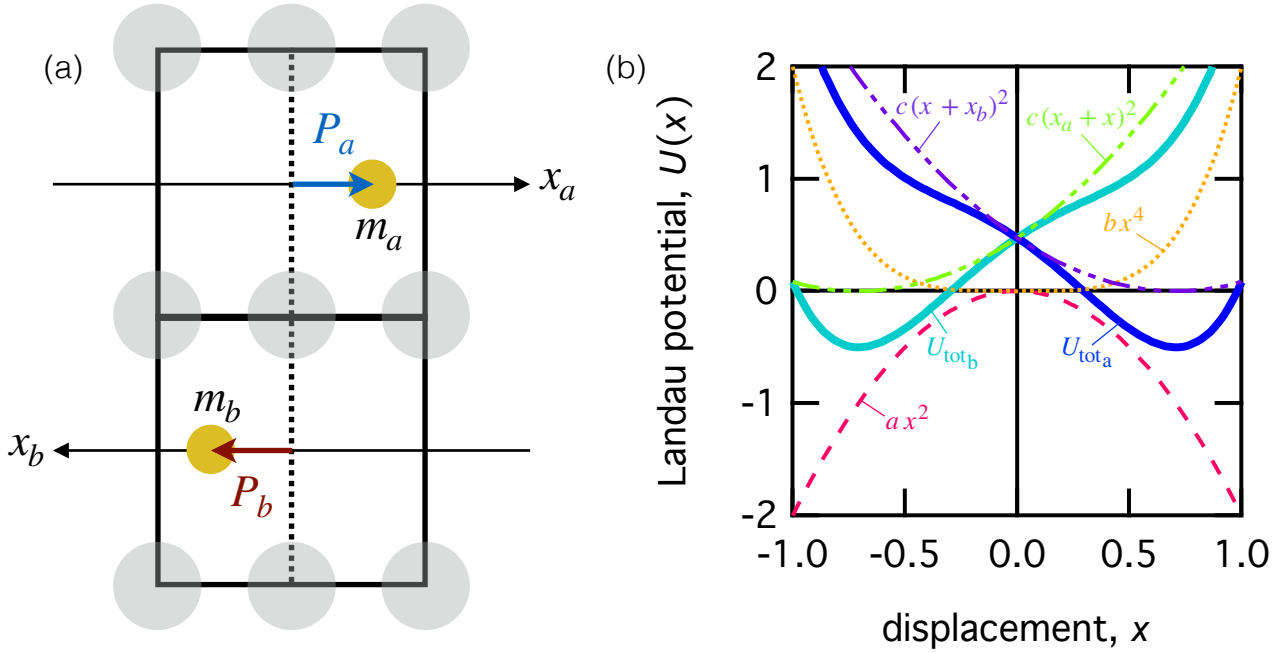

FIG. 1. (a) Schematic of antiferroelectric displacement. The masses m_a=m_b behave independently in the local potential (Eq. 1), interacting only through the model potential (Eqs. 2 and 3). (b) Landau potetial in antiferroelectric configuration ($x_a = -x_b$) as described by Eqs. 1 and 3. For demonstration purposes, the relationship between the different coefficients is set to $-a = b = 2c$.

documented as a description for displacive ferroelectric transitions. Following Kittel's theory of antiferroelectric crystals [1], the spontaneous sublattice polarizations in the antiferroelectric case can be defined as $P_a = qx_an$ and $P_b = qx_bn$, where q is the displaced charge relative to a static oppositely charged background and n is its density.

To solve for the dynamics of the ordered phase, we perform a Taylor expansion around equilibrium by defining $x_a = x_a^0 + \xi_a$ and $x_b = x_b^0 + \xi_b$, where $\xi_{a,b}$ represent small displacements away from equilibrium. Thus,

$$\begin{aligned}
\frac{\partial U_{\mathrm{tot}}}{\partial x_a} &= (x_a^0+\xi_a)\left(2a + 4b(x_a^0+\xi_a)^2\right) + 2c(\underbrace{x_a^0 \mp x_b^0}_{=0} + \xi_a \mp \xi_b),\\
&= (x_a^0+\xi_a)(\underbrace{2a + 4b{x_a^0}^2}_{=0\ \text{(Eq. 9)}} + 8bx_a^0\xi_a) + 2c(\xi_a \mp \xi_b),\\
&= 8b\ \underbrace{{x_a^0}^2}_{=\frac{-a}{2b}\ \text{(Eq. 9)}}\ \xi_a + \underbrace{8bx_a^0\xi_a^2}_{\approx 0} + 2c(\xi_a \mp \xi_b),\\
&= -4a\xi_a + 2c(\xi_a \mp \xi_b). \qquad (10)
\end{aligned}$$

Similarly,

$$\begin{aligned}
\frac{\partial U_{\mathrm{tot}}}{\partial x_b} &= -4a\xi_b \mp 2c(\underbrace{x_a^0 \mp x_b^0}_{=0} + \xi_a \mp \xi_b),\\
&= -4a\xi_b \mp \underbrace{2c(\xi_a \mp \xi_b)}_{\mp 2c\xi_a + 2c\xi_b},\\
&= -4a\xi_b + 2c(\xi_b \mp \xi_a). \qquad (11)
\end{aligned}$$

We look for eigen modes of the form $\ddot{x} = -\omega^2 x$, equivalently $\ddot{\xi} = -\omega^2\xi$. Substituting into Eqs. 4 and 5, this gives,

$$-m\omega^2\xi_a = (-\gamma_a\omega\xi_a) + 4a\xi_a - 2c(\xi_a \mp \xi_b), \qquad (12)$$

$$-m\omega^2\xi_b = (-\gamma_b\omega\xi_b) + 4a\xi_a - 2c(\xi_b \mp \xi_a). \qquad (13)$$

TABLE I. Eigen modes for polar and antipolar oscillations in "ordered" system ($T < T_c$) with ferro- or antiferroelectric interaction.

interaction \ mode	polar	antipolar
ferro	$m\omega_F^2 = -4a$	$m\omega_{AF}^2 = -4a + 4c$
antiferro	$m\omega_F^2 = -4a + 4c$	$m\omega_{AF}^2 = -4a$

Once again neglecting damping, Eqs. 12 and 13 simplify to,

$$(-m\omega^2 - 4a + 2c)\xi_a \mp 2c\xi_b = 0, \tag{14}$$
$$\mp 2c\xi_a + (-m\omega^2 - 4a + 2c)\xi_b = 0, \tag{15}$$

with the solutions,

$$\begin{aligned}(-m\omega^2 - 4a + 2c)^2 - (\mp 2c)(\mp 2c) &= 0\\ (-m\omega^2 - 4a + 2c)^2 &= 4c^2,\\ -m\omega^2 - 4a + 2c &= \pm 2c.\end{aligned} \tag{16}$$

When substituting back into Eqs. 14 and 15, the solution $-m\omega^2 - 4a + 2c = 2c$ or $m\omega^2 = -4a$ gives,

$$\begin{aligned}2c\xi_a \mp 2c\xi_b &= 0,\\ \mp 2c\xi_a + 2c\xi_b &= 0.\end{aligned}$$

For the ferroelectric case (taking the "$-$" operation above) this solution gives $\xi_a = \xi_b$, i.e. in-phase oscillations of the two masses – a polar or "ferroelectric" mode (ω_F). For the antiferroelectric case (taking the "$+$" operation) this solution gives $\xi_a = -\xi_b$, i.e. out-of-phase oscillations of the two masses – an antipolar or "antiferroelectric" mode (ω_{AF}).

Similarly, taking the solution $-m\omega^2 - 4a + 2c = -2c$, or $m\omega^2 = -4a + 4c$ for Eq. 16 gives,

$$\begin{aligned}-2c\xi_a \mp 2c\xi_b &= 0,\\ \mp 2c\xi_a - 2c\xi_b &= 0,\end{aligned}$$

which for the ferroelectric case, results in $\xi_a = -\xi_b$ (antipolar mode). For the antiferroelectric case, we get $\xi_a = \xi_b$ (polar mode). A summary of each of the eigen modes for each interaction (ferro or antiferroelectric) is given in table I.

We now consider the paraelectric case where $x_a = x_b = 0$, such that for small displacements,

$$\frac{\partial U_{tot}}{\partial x_a} = \frac{\partial U_{tot}}{\partial \xi_a} = 2a\xi_a + 2c(\xi_a \mp \xi_b), \tag{17}$$
$$\begin{aligned}\frac{\partial U_{tot}}{\partial x_b} = \frac{\partial U_{tot}}{\partial \xi_b} &= 2a\xi_b \mp 2c(\xi_a \mp \xi_b),\\ &= 2a\xi_b + 2c(\xi_b \mp \xi_a).\end{aligned} \tag{18}$$

Here again the order of the signs refers to the case of ferroelectric and antiferroelectric interactions respectively. Following the same procedure as above, the eigen modes are defined by the two equations,

$$-m\omega^2\xi_a = -2a\xi_a - 2c(\xi_a \mp \xi_b), \tag{19}$$
$$-m\omega^2\xi_b = -2a\xi_b - 2c(\xi_b \mp \xi_a). \tag{20}$$

This simplifies to,

$$\left(-m\omega^2 + 2a + 2c\right)\xi_a \mp 2c\xi_b = 0, \tag{21}$$
$$\mp 2c\xi_a + \left(-m\omega^2 + 2a + 2c\right)\xi_b = 0, \tag{22}$$

with the solutions $-m\omega^2 + 2a + 2c = \pm 2c$.

TABLE II. Eigen modes for polar and antipolar oscillations in paraelectric system ($T > T_c$) with ferro- or antiferroelectric interaction.

mode / interaction	polar	antipolar
ferro	$m\omega_F^2 = 2a$	$m\omega_{AF}^2 = 2a + 4c$
antiferro	$m\omega_F^2 = 2a + 4c$	$m\omega_{AF}^2 = 2a$

The eigen modes are then extracted by classifying the solution with respect to the relationship between ξ_a and ξ_b for ferroelectric and antiferroelectric interactions as was done earlier for the ordered case. The results are summarised in Table II.

In the paraelectric phase we find the same relationship between the polar and antipolar modes for each interaction (namely, $\omega_F^2 - \omega_{AF}^2 \propto c$). Furthermore, a comparison with Table I reveals that the ratio of the slope of the soft modes in the ordered state relative to the paraelectric state should be equal to -2.

Finally, we can use the relationship between the soft mode energies and the strength of the local potential in order to determine an approximate electric poling field strength required to polarize the antiferroelectric state, inducing ferroelectric or ferrielectric order. Electrostatics tells us that locally the potential energy of a single dipole making up the sublattice polarization is given by,

$$U_{\text{dip}} = -\mathbf{p} \cdot \mathbf{E}, \tag{23}$$

Where $\mathbf{p}$ is the electric dipole moment and $\mathbf{E}$ is an external electric field. Considering our simple one-dimensional model, this simplifies to,

$$U_{\text{dip}} = -qxE. \tag{24}$$

In the model potential described above, $a = 0$ at $T = T_c$. Such that the local potential for the displaced ions is primarily described by the effective interaction potential $U_{\text{loc}} \approx cx^2$, with $m\omega_F^2 = 4c$. Thus, equating these two potentials we can solve for E giving,

$$\begin{aligned} -qxE &= \frac{m\omega_F^2 x^2}{4}, \\ E &= -\frac{m\omega_F^2 x}{4q}. \end{aligned} \tag{25}$$

In francisite, the primary ionic displacement at T_c is a $\sim$0.196 Å shift of the Cl^- ions along the $\hat{a}$ axis [2]. Substituting a mass of $34m_{\text{proton}}$ and charge of $-e$ for the Cl ions, with a soft-mode frequency of 0.84 THz at 118 K gives a poling field of $E \approx 1.2$ MV/m.

SPECTROSCOPIC EXPERIMENTAL DETAILS

FTIR – Reflectivity measurements were performed at near-normal incidence (angle of incidence ∼11°) in a Vertex V80 Fourier-transform infrared (FTIR) interferometer. Far-infrared radiation from a Hg-lamp source, reflected by the sample, was detected using a 4.2 K Si bolometer. The infrared polarization was controlled by a rotational linear gold-wire-grid polarizer positioned before the sample. The sample was mounted on a copper plate with adjustable height inside of an Oxford Insturments helium-flow cryostat with polypropylene optical windows. A 7 mm diameter gold mirror reference was positioned below the sample and could be moved into the beam path by adjusting the height of the copper mount. An aperture in front of the source ensured a incident spot size of 2 mm confined within boundaries of the sample and reference surfaces. Measurements were performed from 10-300 K with references taken at each temperature setting. In this setup, a spectral bandwidth of 40-900 cm^{-1} was achieved.

THz – Phase sensitive THz transmission measurements were performed using a Mach-Zehnder interferometer incorporating a backward-wave oscillator source and 4.2 K Si bolometer detector. Two different sources were used to cover the spectral range from 8-15 cm^{-1} and 20-28 cm^{-1}. The radiation was focused using polypropylene lenses and its polarization was controlled by wire-grid linear polarizers. The sample was mounted on mylar film attached to a copper plate with a 4 mm aperture inside of an oxford instruments 7-T magneto-optical cryostat. Transmission references were obtained by moving the sample out of the beam-path aligned to the 4 mm aperture. Phase sensitivity is achieved by recording the path difference of the beam passing through the sample compared to a reference beam passing outside the cryostat. Temperature dependent measurements were performed from 10-300 K with references obtained for each temperature setting.

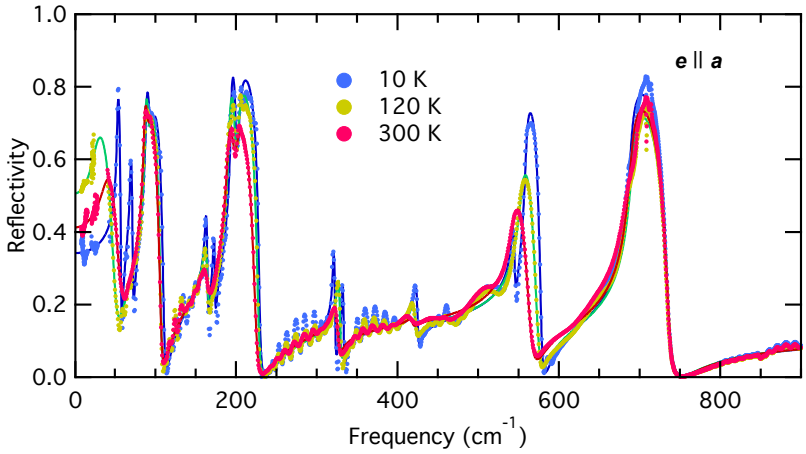

FIG. 2. Broadband far-infrared reflectivity of $Cu_3Bi(SeO_3)_2O_2Cl$ for $\mathbf{e}||\hat{a}$. Solid lines partly hidden by the experimental data points are theoretical fits as described in the main text. Data points from 40–900 cm^{-1} are the experimental results of the FTIR measurements performed in reflection. Data points from 8–28 cm^{-1} are the experimental results from the Mach-Zehnder interferometer performed in transmission.

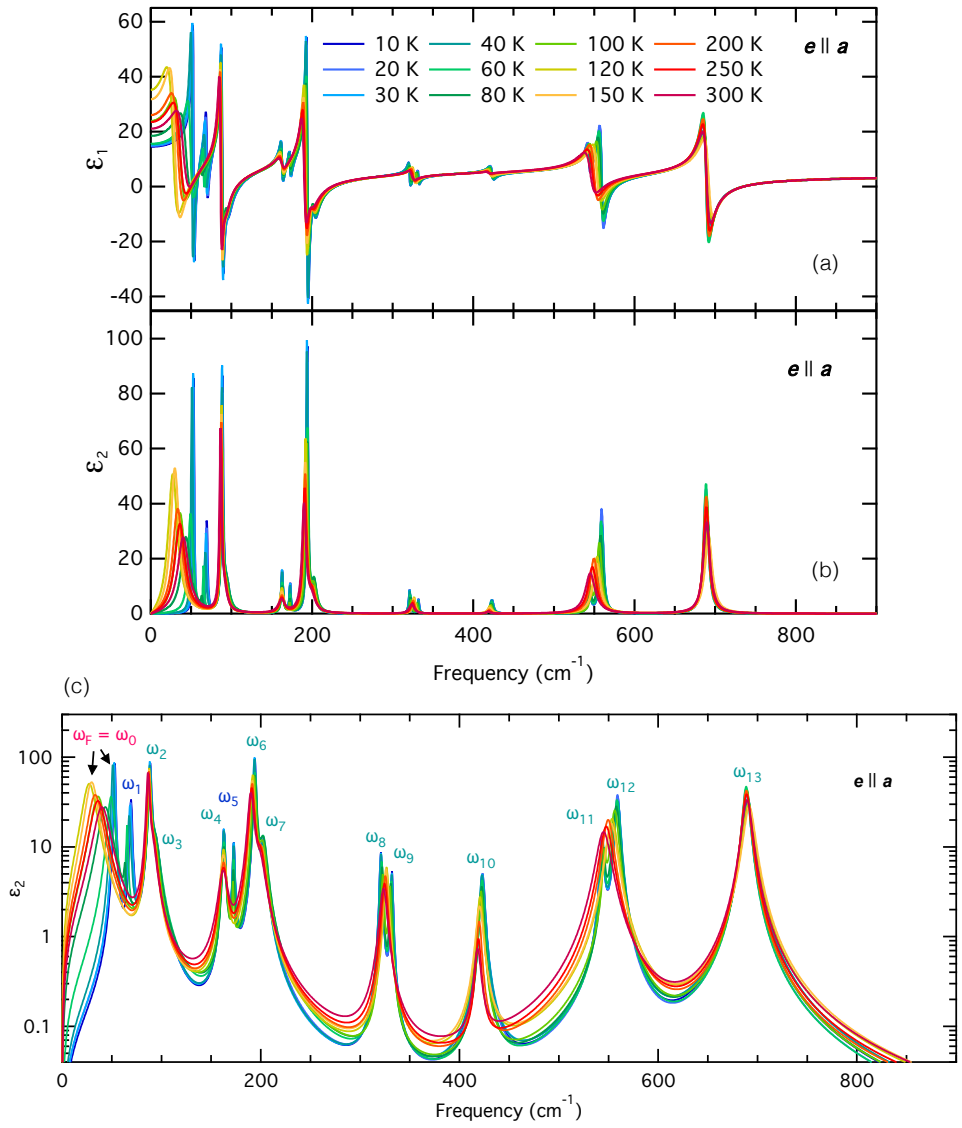

FIG. 3. (a) Real and (b) imaginary components of the dielectric response due to phonon contributions in the $\hat{a}$ direction. Curves are extracted using a Lorentz oscillator model fit to the reflectivity as discussed in the main article and above. (c) Shows the imaginary response in a logarithmic scale highlighting the different phonon modes. Labels in red (ferroelectric soft mode) and teal are phonons that appear at all temperatures, labels in blue appear only below T_c.

CAPACITIVE MEASUREMENT DETAILS

Temperature dependent capacitive measurements were carried out on a single crystal sample, with dimensions $\sim$4×5×1.5 mm^3. Silver paint electrodes were applied to the narrow edges of the sample as shown in Fig. 4. The measurements were performed using an Alpha-analyzer integrated within a Quantum Design Physical Property Measurement System (PPMS). An ac field of 1 V (rms) with frequencies from 1 Hz, to 100 kHz was applied while the Alpha-analyser recorded the capacitance as a function of temperature for heating and cooling cycles between 5 K and 300 K at a rate of 0.2 K/min. No significant temperature hysteresis was observed.

The complex capacitive measurements are shown in Figs. 4 (a) and (b). Apart from the clear dielectric anomaly at the antiferroelectric transition, we also observe a strong increase in the capacitance at high temperatures and low voltage frequencies. This anomalous signal is a result of a small conductivity of the sample that emerges at high temperatures. Often referred to as *Maxwell-Wagner polarization* [3], it is an interfacial effect that appears due to a build up of charge at the electrode-sample junction, contributing an additional capacitance and resistance at the interface. The feature is dominant at low frequencies, disappearing at frequencies on the order of 100 kHz.

TABLE III. Fitted oscillator parameters for $Cu_3Bi(SeO_3)_2O_2Cl$ in the $\hat{a}$ direction at 10 K and 300 K.

	$\mathbf{e}\|\|\hat{a}$: 10 K			$\mathbf{e}\|\|\hat{a}$: 300 K		
	$\Delta\varepsilon$	ω (cm^{-1})	γ (cm^{-1})	$\Delta\varepsilon$	ω (cm^{-1})	γ (cm^{-1})
ω_0	3.018	52.9	1.85	11.180	40.9	16.69
ω_1	1.140	69.3	2.40	–	–	–
ω_2	2.462	88.6	2.62	2.246	86.3	3.07
ω_3	0.841	94.4	8.58	0.719	91.0	8.92
ω_4	0.271	162.7	2.85	0.284	162.0	9.65
ω_5	0.134	172.2	2.20	–	–	–
ω_6	1.156	193.9	2.33	1.214	190.0	5.95
ω_7	0.328	202.5	6.42	0.298	199.0	11.24
ω_8	0.068	320.8	2.51	0.077	323.3	7.33
ω_9	0.034	332.0	2.17	–	–	–
ω_{10}	0.054	423.1	4.55	0.010	418.1	6.53
ω_{11}	0.086	543.3	3.89	–	–	–
ω_{12}	0.319	559.1	4.93	0.397	545.0	14.73
ω_{13}	0.462	689.1	7.94	0.482	689.3	10.00

Typically, capacitance can be used to determine a sample's permittivity by assuming a three-dimensional plane-parallel plate capacitor geometry where,

$$C = \frac{\varepsilon\varepsilon_0 S}{d}; \quad \varepsilon = \frac{Cd}{\varepsilon_0 S}. \tag{26}$$

Here C is the capacitance, ε_0 is the permittivity of free space, d is the distance between the two parallel plate electrodes and S is their surface area. As is clear in Fig. 4, the electrode geometry used for our measurements is not well represented by a three-dimensional plane-parallel plate. Specifically, the sample morphology dictates $d >> S$ with a geometry more representing two parallel strips rather than plates. As such, we would expect that there will be a non-negligible amount of stray fields that sample both the outer vacuum and other crystal directions when we measure the capacitance. Thus equation 26 is not a strictly valid conversion for our data.

Alternatively, the experimental permittivity can be determined using the following expression,

$$\varepsilon = \frac{C}{\zeta}\frac{d}{\varepsilon_0 S}, \tag{27}$$

where ζ is a geometric calibration factor determined using a finite element analysis as detailed in the section below. This calibration factor takes into account the anisotropy of the sample and the non-plane–parallel geometry of the electrodes. Its value is dependent on the actual permittivity along the direction of measurement so we have calculated it for several values of ε_a shown in Table IV. The calculated permittivity in Fig. 4 (c) was obtained using equation 27, a calibration factor $\zeta = 1.89$ and electrode distance $d = 3.95\,\text{mm}$. Since the variation in electrode surface area is taken into account by the finite element analysis and hence enters equation 27 through ζ, we use an average approximation of $S = 1\,\text{mm}^2$ in the calculation.

The value of $\zeta(\varepsilon_a = 25) = 1.89$ is chosen as a representative average value for $\varepsilon_a(T)$. Approximate values for ε_b and ε_c are obtained from other capacitive measurements. Since the single crystal samples grow naturally as plates with primary surfaces normal to $\hat{c}$, determining ε_c by capacitive measurements and equation 26 is relatively straight forward. This was done previously and published in Ref. [2]. The result at 100 kHz between 0-250 K is shown in Fig. 6. As can be seen $\varepsilon_c(T) \approx 15$ remains fairly constant across the temperature span investigated.

The $\hat{b}$ direction is less trivial. Due to the morphology of the sample, constructing an electrode setup with parallel surfaces normal to $\hat{b}$ was impractical. Therefore we have measured the capacitance using the electrode setup depicted in Fig. 5 (d). The results are presented in Figs. 5 (a) and (b). The real component of capacitance bares little resemblance to the results for $\mathbf{E}||\hat{a}$ or $\mathbf{E}||\hat{c}$ so we can be confident that the measurements primarily sample the $\hat{b}$ direction. An approximate value for ε_b is obtained using the following expression,

$$\varepsilon_b = \alpha\frac{C}{\varepsilon_0}, \tag{28}$$

where $\alpha = 2574$ is a scaling factor. The scaling factor was determined by assuming an expected value of $\varepsilon_b(300\,\text{K}) = 15$, obtained by extrapolating a reflectivity measurement shown in Fig. 5 (e) with $R(\omega = 0) \approx 0.35$. The variation of

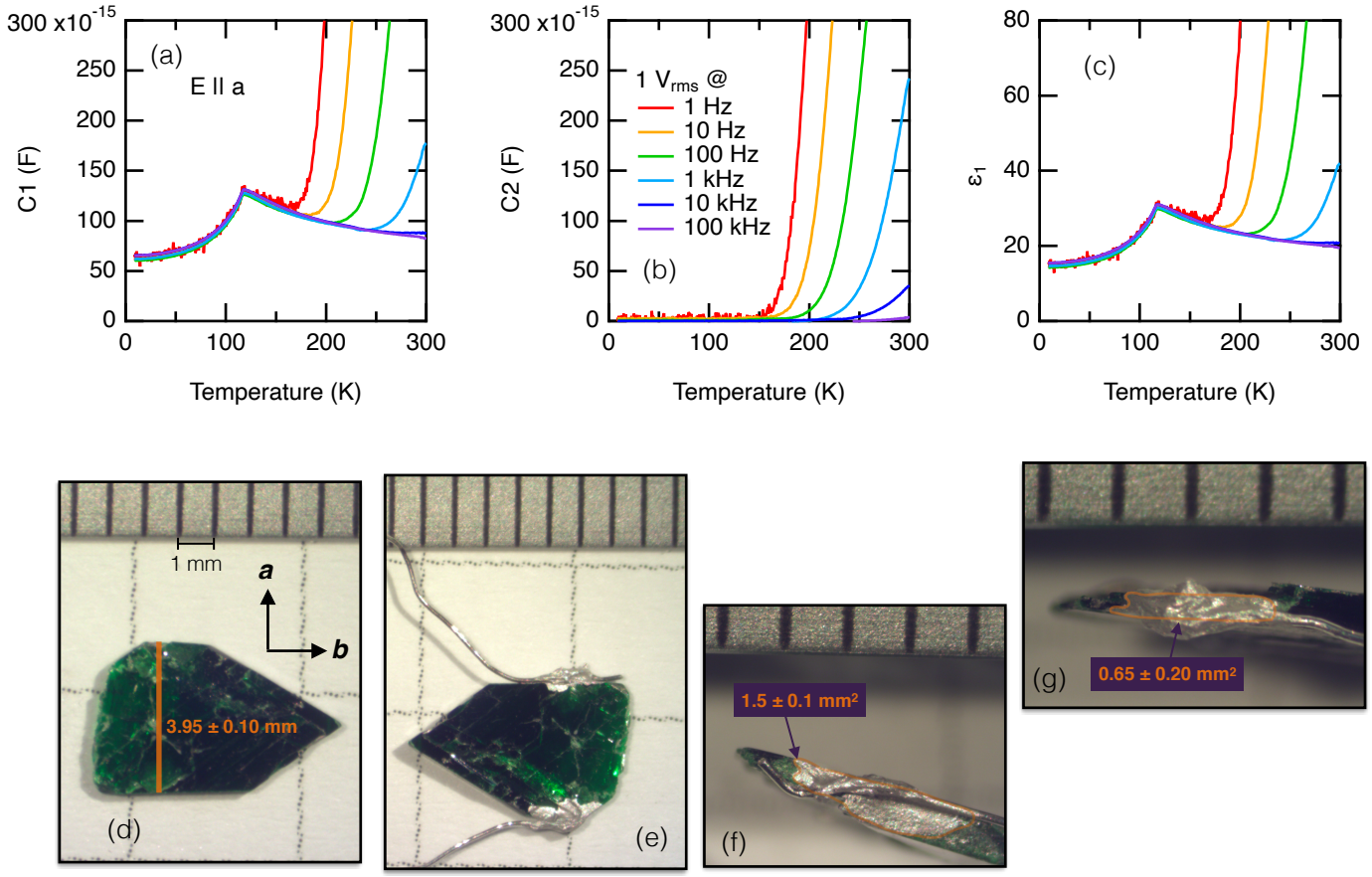

FIG. 4. Real (a) and imaginary (b) capacitance measurements for $\mathbf{E}||\hat{a}$, where $C = C1 - iC2$. (c) Permittivity calculated using equation 27 with $d = 3.95\,\mathrm{mm}$, $S = 1\,\mathrm{mm}^2$ and $\zeta = 1.89$. (d) Single crystal with close-to-parallel surfaces normal to $\hat{a}$ direction. (e) Electrode arrangement for $\mathbf{E}||\hat{a}$ configuration. (f, g) Surface area of the two close-to-parallel electrodes.

ε_a	10	15	20	25	30	35	40
$\zeta\|_{\varepsilon_b=15}$	2.54	2.16	1.95	1.82	1.72	1.65	1.59
$\zeta\|_{\varepsilon_b=18}$	2.71	2.27	2.04	1.89	1.78	1.70	1.64

TABLE IV. Geometric calibration factors (ζ) for different values of dielectric permittivity along $\hat{a}$ (ε_a) and $\hat{b}$ (ε_b). Results determined by finite element analysis.

$\varepsilon_b(T)$ is small compared to $\varepsilon_a(T)$ increasing from $\varepsilon_b(300\,\mathrm{K}) = 15$ to $\varepsilon_b(5\,\mathrm{K}) = 19$. Flattening off at lower temperature, the average value can be considered $\varepsilon_b(T) \approx 18$.

When calculating ζ for the ε_a measurements, average values of $\varepsilon_a = 25$, $\varepsilon_b = 18$, and $\varepsilon_c =$ were used, giving $\zeta = 1.89$. In the main article, and in Fig. 6, we also show high and low limits that take the changes in ε_a and ε_b into account. These are $\zeta(\varepsilon_a = 35, \varepsilon_b = 15) = 1.65$ and $\zeta(\varepsilon_a = 15, \varepsilon_b = 18) = 2.27$ for the high and low limit respectively. The limits represent the maximum and minimum permittivity values expected across the full temperature span and therefore act as an uncertainty in the measured value of $\varepsilon_a(T)$. As is evident in the main article, our infrared results fall nicely within these limits.

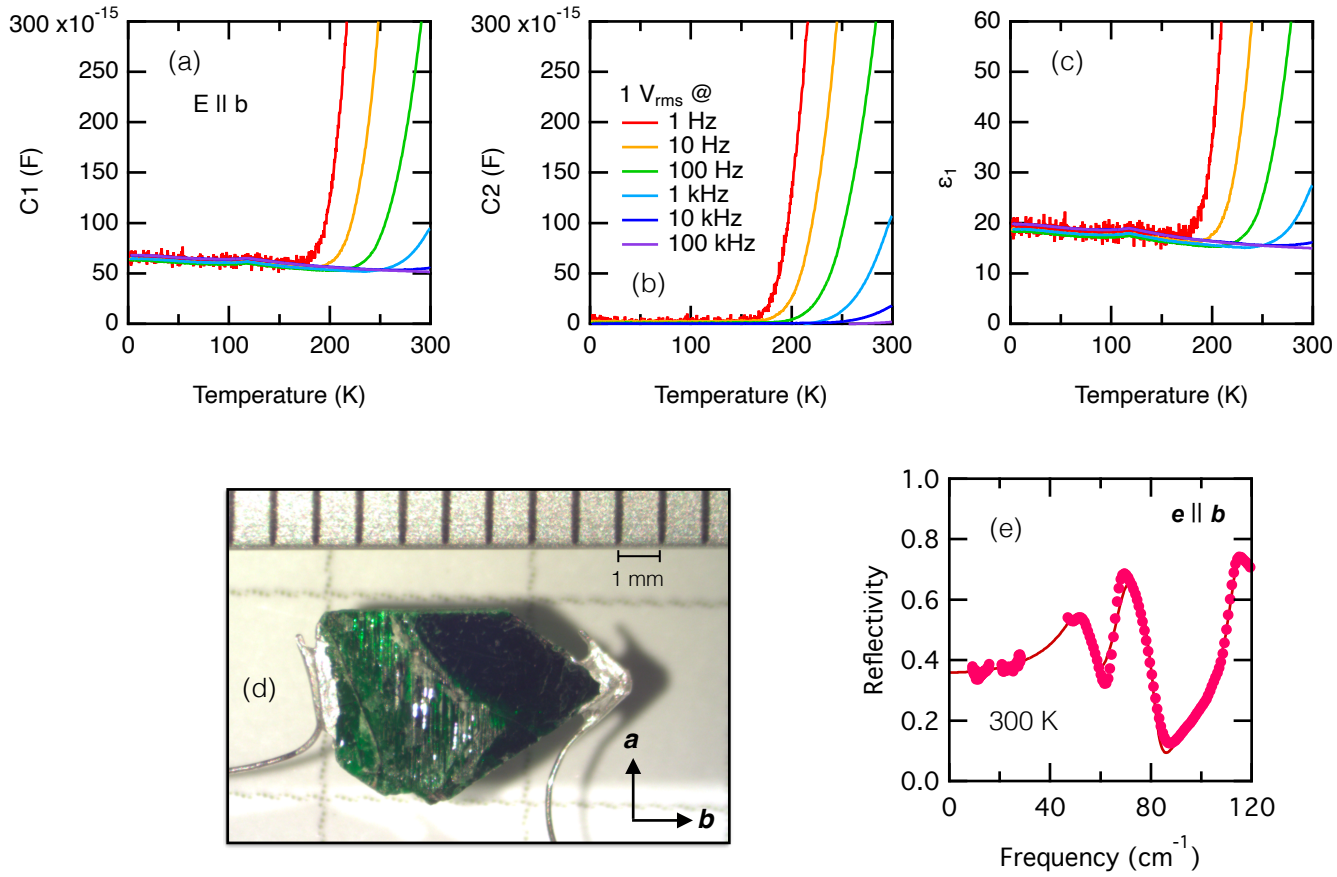

FIG. 5. Real (a) and imaginary (b) capacitance measurements for $\mathbf{E}||\hat{b}$, where $C = C1 - iC2$. (c) Permittivity calculated using equation 28 with $\alpha = 2574$. (d) Electrode arrangement for $\mathbf{E}||\hat{b}$ configuration, note non-parallel nature of electrodes. (e) Reflectivity of francisite at 300 K for radiation polarised along the $\hat{b}$ axis.

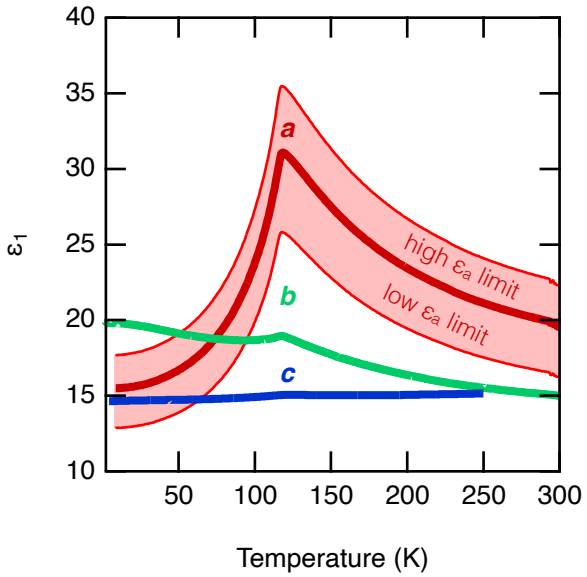

FIG. 6. Anisotropy of dielectric permittivity. ε_a and ε_b were obtained from capacitive measurements performed with a 1.0 V_{rms} 100 kHz oscillating voltage. ε_c is adapted from Ref. [2] and obtained from capacitive measurements using a 1.0 V_{rms} 100 kHz oscillating voltage.

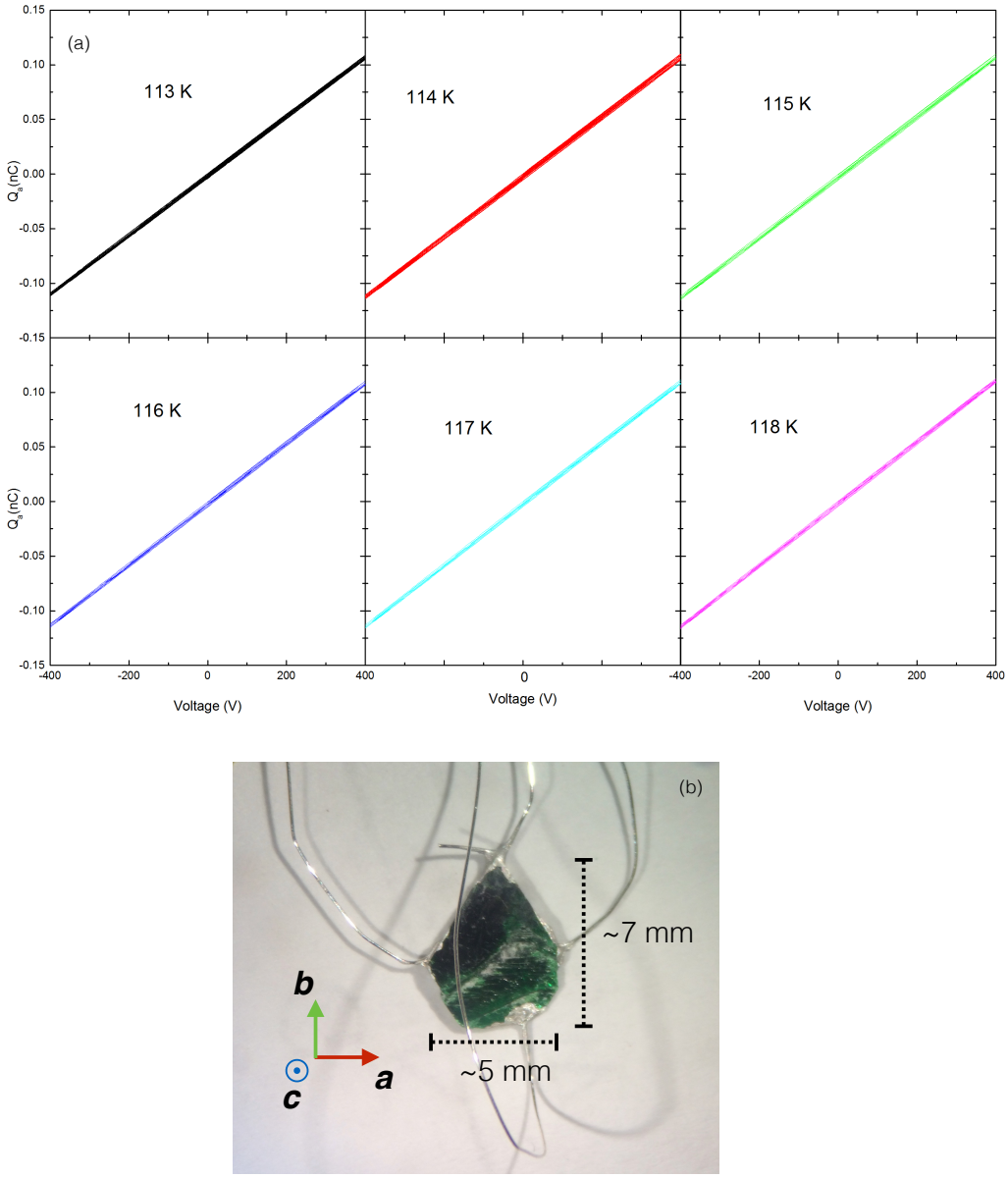

FIG. 7. (a) Electric-field induced charge measurements of $Cu_3Bi(SeO_3)_2O_2Cl$ for $\mathbf{E}||\hat{a}$ at different temperatures approaching the critical temperature (118 K). Voltages were applied over 5 mm across the sample shown in (b). No meta-electric transition is observed that would suggest an electric field induced ferroelectric phase. Electrical discharge around the sample limited the maximum voltage that could be applied. Higher voltages in the range of 1 MV/m (eg. 1 kV across a 1 mm thick sample) are likely required to induce the ferroelectric phase.

FINITE ELEMENT ANALYSIS

The governing equation of the electrostatic problem is: $\operatorname{div}\mathbf{D} = \operatorname{div}\hat{\varepsilon}\mathbf{E} = 4\pi\rho$. (Gauss units are assumed througout this section, however, the final result is dimensionless and is applicable in any unit system.) Introducing the scalar potential φ, so that $\mathbf{E} = -\nabla\varphi$, we obtain the equation $-\operatorname{div}\hat{\varepsilon}\nabla\varphi = 4\pi\rho$. The weak form is obtained in a standard way by multiplying with the test function ψ and integrating over the whole computational domain:

$$-\int_\Omega \psi \operatorname{div}\hat{\varepsilon}\nabla\varphi\, d\Omega = \int_\Omega 4\pi\rho\psi\, d\Omega.$$

From the identity $\operatorname{div}\psi\,\hat{\varepsilon}\nabla\varphi = \nabla\psi\cdot\hat{\varepsilon}\cdot\nabla\varphi + \psi\operatorname{div}\hat{\varepsilon}\nabla\varphi$ and the divergence theorem we have:

$$\int\limits_{\Omega} \nabla\psi\cdot\hat{\varepsilon}\cdot\nabla\varphi\,d\Omega - \int\limits_{\partial\Omega}\psi\hat{\varepsilon}\nabla\varphi\cdot d\mathbf{S} = \int\limits_{\Omega} 4\pi\rho\psi\,d\Omega.$$

The term $\hat{\varepsilon}\nabla\varphi\cdot d\mathbf{S} = -\mathbf{D}\cdot\mathbf{n}\,dS = -D_n\,dS$ so we have a surface integral over the normal component of the $\mathbf{D}$ field:

$$\int\limits_{\Omega} \nabla\psi\cdot\hat{\varepsilon}\cdot\nabla\varphi\,d\Omega + \int\limits_{\partial\Omega}\psi D_n\,dS = \int\limits_{\Omega} 4\pi\rho\psi\,d\Omega.$$

The current problem is solved without charge density distribution, $\rho = 0$. The fixed potential of the electrodes φ_D is set by the penalty-type Robin boundary conditions, $D_n = k(\varphi - \varphi_D)$ in order to soften the field divergence at the sharp metal edges (the constant k is chosen to be large, see below). The final equation is then:

$$\int\limits_{\Omega} \nabla\psi\cdot\hat{\varepsilon}\cdot\nabla\varphi\,d\Omega + \int\limits_{\partial\Omega} k\psi\varphi\,dS = \int\limits_{\partial\Omega} k\psi\varphi_D\,dS.$$

The boundary conditions are fixed potential $\varphi_D = \varphi_+ = +\varphi_0/2$ on one electrode, $\varphi_D = \varphi_- = -\varphi_0/2$ on the other electrode and natural homogeneous Neumann condition $D_n = 0$ on the outer computational domain border. Setting the outer domain boundary to zero potential $\varphi = 0$ is also possible and gives the same results as the current approach.

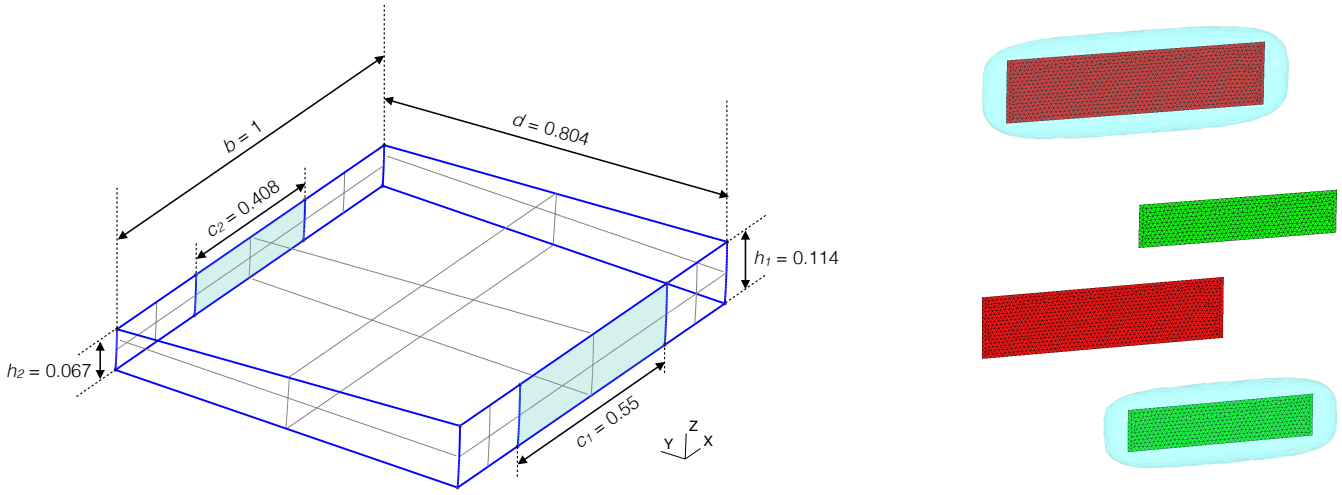

FIG. 8. Left panel: simplified 3D model of the sample. All dimensions are normalized to the effective width of the sample $b = 4.91$ mm. Right panels: virtual charge integration surfaces for positive (large red) and negative (small green) electrodes.

The problem is now reformulated in the dimensionless form by normalizing all dimensions to the effective width of the sample b, see left panel of Fig. 8. This leads to the following transformation rules:

$$d\Omega = b^3 d\tilde{\Omega}, \qquad dS = b^2 d\tilde{S}, \qquad \nabla_x\varphi = \frac{\nabla_\xi\varphi}{b}.$$

The potential $\varphi = \varphi_0\,\tilde{\varphi}$ is also represented as the scaling potential φ_0 times the dimensionless potential $\tilde{\varphi}$, which changes by 1 from one electrode to another. The dimensionless weak form of the problem is then:

$$\int\limits_{\tilde{\Omega}} \nabla_\xi\tilde{\psi}\cdot\hat{\varepsilon}\cdot\nabla_\xi\tilde{\varphi}\,d\tilde{\Omega} + \int\limits_{\partial\tilde{\Omega}}\beta\tilde{\psi}\tilde{\varphi}\,d\tilde{S} = \int\limits_{\partial\tilde{\Omega}}\beta\tilde{\psi}\tilde{\varphi}_D\,d\tilde{S}, \tag{29}$$

where $\beta = bk$ is a dimensionless constant. Its value in the present work is set to $\beta = 10^5$.

The main post-processing result apart from the visual inspection of the field distribution is the total charge Q accumulated on each of the electrodes. By definition, the capacitance C is the ratio of the charge on one of the

electrodes to the potential difference between the electrodes: $C = Q/\varphi_0$. The charge is computed from the Gauss theorem by integrating the electric displacement $\mathbf{D}$:

$$Q = \frac{1}{4\pi}\int\limits_{\partial V} D_n\, dS = -\frac{1}{4\pi}\int\limits_{\partial V} \hat{\varepsilon}\nabla_x\varphi\cdot\mathbf{n}\, dS = -\frac{1}{4\pi}\int\limits_{\partial \tilde{V}} \frac{\hat{\varepsilon}}{b}\nabla_\xi(\varphi_0\tilde{\varphi})\cdot\tilde{\mathbf{n}}\, b^2\, d\tilde{S} = \frac{\varphi_0 b}{4\pi}\int\limits_{\partial \tilde{V}} \tilde{D}_n\, d\tilde{S},$$

where the virtual integration surface $\partial\tilde{V}$ is taken around the electrode in its close vicinity and is defined by an isosurface of a special scalar field fitted to each of the electrodes, see right panels of Fig. 8. The dimensionless capacitance normalized to the width of the sample b is then:

$$\tilde{C} = \frac{C}{b} = \frac{Q}{\varphi_0 b} = \frac{1}{4\pi(\tilde{\varphi}_+ - \tilde{\varphi}_-)}\int\limits_{\partial \tilde{V}} \tilde{D}_n\, d\tilde{S}.$$

The normalized potential difference $(\tilde{\varphi}_+ - \tilde{\varphi}_-)$ should be exactly 1 for Dirichlet boundary conditions. In the present case it is still computed from the numerical calculations in order to take the small variation of potential due to soft penalty-type Robin boundary conditions into account.

The real sample is modelled by a hexahedron shape, see left panel of Fig. 8. The model captures such features of the real sample as variable thickness in z-direction, different areas of two contacts and that the contacts do not cover the whole face of the sample. The triangular shape of one of the sides of the sample is omitted from the model, because it is rather far from the contacts (see Fig. 4, panel (e)) with a low expected field magnitude, it gives only a small contribution to the total capacitance. Both the 3D model of the sample and the meshing are done using the open-source program `GMSH` [4]. The dielectric permittivity $\hat{\varepsilon}$ is taken to be anisotropic,

$$\hat{\varepsilon} = \begin{pmatrix} \varepsilon_a & 0 & 0 \\ 0 & \varepsilon_b & 0 \\ 0 & 0 & \varepsilon_c \end{pmatrix},$$

with $\varepsilon_b = \varepsilon_x = 18$, $\varepsilon_c = \varepsilon_z = 15$, and $\varepsilon_a = \varepsilon_y$ - variable, see Table IV. The isosurfaces $\partial\tilde{V}$ used to integrate the total charges of each of the electrodes are defined by equations $s_+(x,y,z) = 0$ and $s_-(x,y,z) = 0$, where scalar fields s_+ and s_- are:

$$s_+ = \left(\frac{x}{c_1/2+e}\right)^4 + \left(\frac{y+d/2}{e}\right)^4 + \left(\frac{z}{h_1/2+e}\right)^4 - 1, \qquad s_- = \left(\frac{x}{c_2/2+e}\right)^4 + \left(\frac{y-d/2}{e}\right)^4 + \left(\frac{z}{h_2/2+e}\right)^4 - 1,$$

with $e = 0.05$, see right panels of Fig. 8.

The whole computational domain is subdivided into a tetrahedral mesh, see Fig. 9. The size of the cube around the sample to take effects of stray field into account is set to $a = 10$ (10 times larger than the sample width $b = 1$). Variable size meshing is used to spare elements near the domain boundary on the one hand, and to provide enough resolution close to the edges of the contacts on the other. Note that the smallest elements close to the contacts are taken as 4 times smaller in the mesh used for calculations, compared with the mesh shown in Fig. 9. The total number of elements in the final mesh is reaching 10^6. The finite element implementation is written in `FreeFEM++` finite element framework [5]. Because the system matrix corresponding to the weak form (29) is symmetric, the conjugate gradient iterative method is used to solve the linear system of equations. Note, that using a direct solver leads to prohibitive memory requirements for a problem of this size. Visualization of the solution potential $\tilde{\varphi}$ and electric field $\mathbf{E}$ are done in the open-source program `medit` [6] that is normally shipped with `FreeFEM++`.

One example of the distribution of electric potential $\tilde{\varphi}$ (top panels) and electric field $\mathbf{E}$ (bottom panels) for the value of $\varepsilon_a = 25$ is shown in Fig. 10. One can see that the potential and electric field are distributed quite homogeneously along the height of the sample in the z-direction (middle panels), but are far from the uniform distribution, typical for the parallel plate capacitor, in the x-y-plane of the sample (right panels). Note that the length of arrows in the bottom middle and right panels is proportional to the size of finite elements and not to the magnitude of the electric field $\mathbf{E}$. The magnitude of the field on the surface of the sample is plotted in the bottom left panel of Fig. 10. One can clearly see the divergence of the field near the sharp edges of the contact. It is this divergence that requires the local refinement of the mesh close to the edges and that also precludes the precise direct integration over the surface of the contact to get the total charge Q accumulated on it.

Figure 11 shows the dependence of the dimensionless capacitance $\tilde{C}$ on the dielectric permittivity ε_a (black curve). The red line is the linear dependence of a parallel plate capacitor $\tilde{C} = \tilde{C}_0\,\varepsilon_a$, where $\tilde{C}_0$ is the geometric capacitance

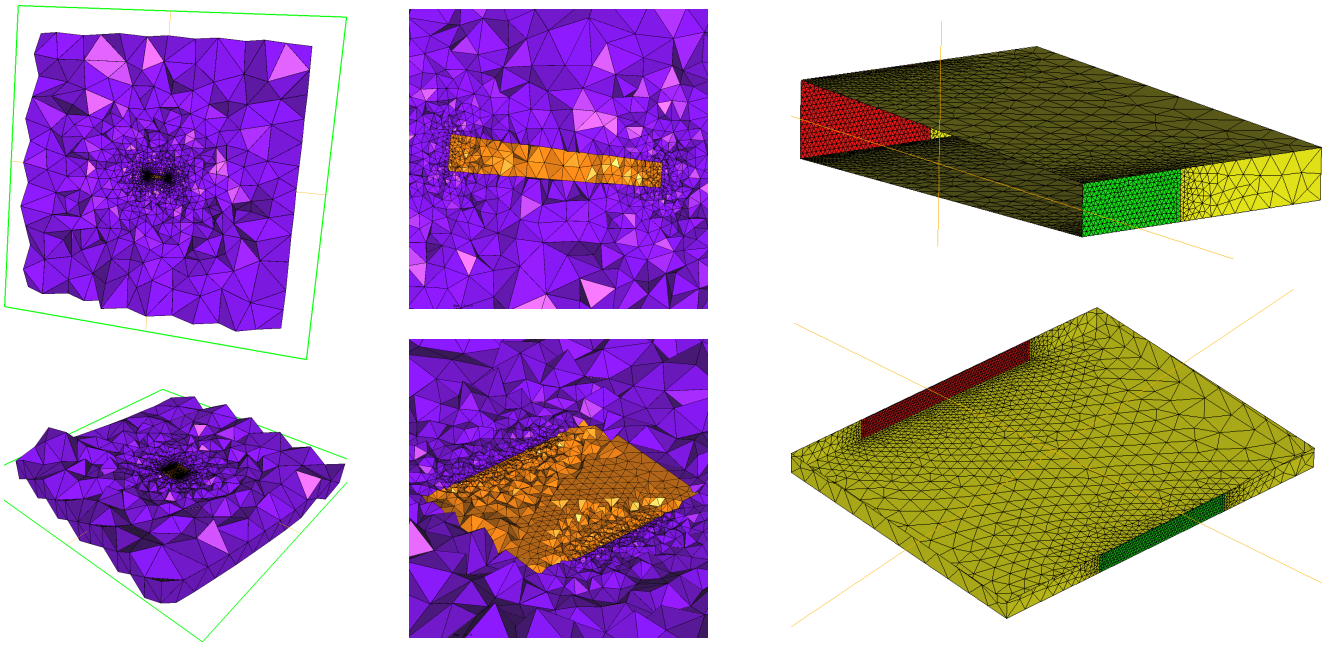

FIG. 9. Details of volumetric 3D (left and middle panels) and surface 2D (right panels) meshing. Top panels demonstrate the cuts of the computational domain by vertical y-z-plane, bottom panels - by horizontal x-y-plane. Left panels give the overview of the meshing of the whole domain, middle and right panels highlight the meshing of the sample.

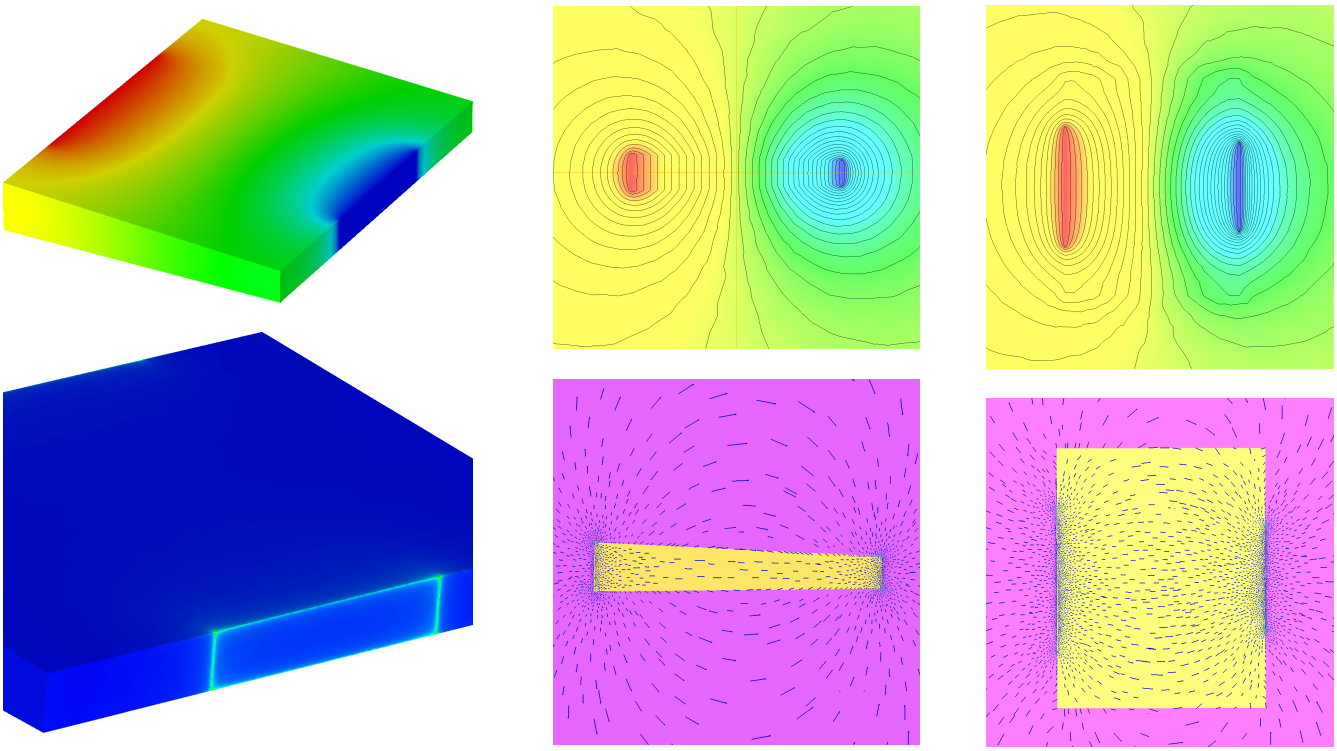

FIG. 10. Distributions of electric potential $\tilde{\varphi}$ (top panels) and electric field $\mathbf{E}$ (bottom panels) around the sample. Left panels give an overview of the distribution of potential and the magnitude of electric field on the surface of the sample. Middle panels show isolines of potential and vector field of $\mathbf{E}$ in the vertical y-z-plane, right panels - in the horizontal x-y-plane.

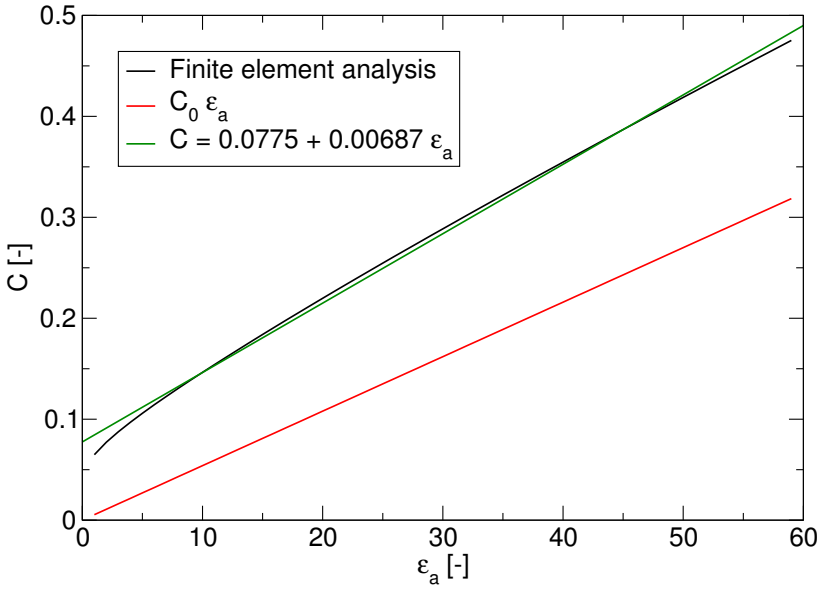

FIG. 11. Dimensionless capacitance $\tilde{C}$ as a function of ε_a. The black curve shows results of the finite element analysis, the red line is the capacitance of a parallel plate capacitor and the green line is a linear fit of the finite element results.

without any material ($\varepsilon = 1$):

$$\tilde{C}_0 = \frac{S}{4\pi d} = 0.00539878.$$

The contact area S is calculated from the averaged parameters of both contacts: $S = c\,h$, with $c = (c_1 + c_2)/2$ and $h = (h_1 + h_2)/2$. The deviation of the calculated 3D capacitance from the parallel plate formula is obvious. One can try to decompose the real capacitance into the stray capacitance $\tilde{C}_1$ due to electric field outside the sample and the internal capacitance $\tilde{C}_2\,\varepsilon_a$: $\tilde{C} = \tilde{C}_1 + \tilde{C}_2\,\varepsilon_a$. The result of the best fit is shown in Fig. 11 by a green line. One can see that the dependence of a total capacitance $\tilde{C}(\varepsilon_a)$ is not linear and the above approximation does not work well. Therefore, a permittivity dependent correction factor

$$\zeta = \frac{\tilde{C}}{\tilde{C}_0\,\varepsilon_a}$$

is used instead to correct the values of dielectric permittivity calculated from a parallel plate formula (26), see Table IV and formula (27).

* evan.constable@tuwien.ac.at
† mael.guennou@uni.lu

[1] C. Kittel, Theory of Antiferroelectric Crystals, Phys. Rev. Lett. **82**, 729 (1951).
[2] E. Constable, S. Raymond, S. Petit, E. Ressouche, F. Bourdarot, J. Debray, M. Josse, O. Fabelo, H. Berger, S. deBrion and V. Simonet Magnetic and dielectric order in the kagomelike francisite $Cu_3Bi(SeO_3)_2O_2Cl$, Phys. Rev. B **96**, 014413 (2017).
[3] E. Barsoukov and J. R. Macdonald, Impedance Spectroscopy, Wiley (2005).
[4] C. Geuzaine and J.-F. Remacle, Gmsh: A 3-D finite element mesh generator with built-in pre- and post-processing facilities, Int. J. Numer. Methods Eng. **79**, 1309 (2009).
[5] F. Hecht, New development in freefem++, J. Numer. Math. **20**, 251 (2012).
[6] P. Frey, MEDIT : An interactive Mesh visualization Software, INRIA **RT-0253**, 41 (2001).